www.nature.com/scientificreports

SCIENTIFIC REPORTS

natureresearch

Received: 19 February 2019
Accepted: 19 July 2019

Spatial Regulation of Mitochondrial Heterogeneity by Stromal Confinement in Micropatterned Tumor Models

Hydari Masuma Begum[1], Hoang P. Ta[1], Hao Zhou[1], Yuta Ando[1], Diane Kang[2], Kristen Nemes[3], Chelsea F. Mariano[1], Jia Hao[1], Min Yu[2,4] & Keyue Shen[1,4,5]

Heterogeneity of mitochondrial activities in cancer cells exists across different disease stages and even in the same patient, with increased mitochondrial activities associated with invasive cancer phenotypes and circulating tumor cells. Here, we use a micropatterned tumor-stromal assay (μTSA) comprised of MCF-7 breast cancer cells and bone marrow stromal cells (BMSCs) as a model to investigate the role of stromal constraints in altering the mitochondrial activities of cancer cells within the tumor microenvironment (TME). Using microdissection and RNA sequencing, we revealed a differentially regulated pattern of gene expression related to mitochondrial activities and metastatic potential at the tumor-stromal interface. Gene expression was confirmed by immunostaining of mitochondrial mass, and live microscopic imaging of mitochondrial membrane potential ($\Delta\Psi_m$) and optical redox ratio. We demonstrated that physical constraints by the stromal cells play a major role in $\Delta\Psi_m$ heterogeneity, which was positively associated with nuclear translocation of the YAP/TAZ transcriptional co-activators. Importantly, inhibiting actin polymerization and Rho-associated protein kinase disrupted the differential $\Delta\Psi_m$ pattern. In addition, we showed a positive correlation between $\Delta\Psi_m$ level and metastatic burden *in vivo* in mice injected with MDA-MB-231 breast cancer cells. This study supports a new regulatory role for the TME in mitochondrial heterogeneity and metastatic potential.

Despite the latest advances in cancer therapeutics, the five-year survival rate for patients diagnosed with metastatic breast cancer is at a staggering 27% as opposed to 99% for those with localized disease[1]. A better understanding of metastatic progression is therefore crucial to improve prevention and treatment of advanced breast cancer.

Mitochondria have recently emerged as a potential regulator of cancer progression and metastasis. It has been shown that cancer cells depend on mitochondrial respiration for their *in vivo* tumor-forming ability[2–4], and that mitochondrial metabolites play a role in driving oncogenesis[5] and epithelial-mesenchymal transition (EMT)[6], a phenotypic switch that precedes metastasis[7]. Importantly, there is significant heterogeneity in mitochondrial phenotypes across cancer disease stages, and even in the same patient. Increased mitochondrial redox activities in tumors have been correlated with tumor aggressiveness and metastatic potential[8]. Higher mitochondrial membrane potential ($\Delta\Psi_m$) is associated with cancer cell survival and invasiveness[9–12]. In breast cancer, circulating tumor cells (CTCs), the presumptive precursor of metastases, exhibit enhanced mitochondrial biogenesis and respiration compared to cancer cells from primary tumors in the same host[13]. However, questions regarding where and how the heterogeneity of mitochondrial activities arises, and its impact on metastatic development, remain unanswered.

[1]Department of Biomedical Engineering, Viterbi School of Engineering, University of Southern California, Los Angeles, CA, 90089, USA. [2]Department of Stem Cell Biology and Regenerative Medicine, Keck School of Medicine, University of Southern California, Los Angeles, CA, 90033, USA. [3]Mork Family Department of Chemical Engineering, Viterbi School of Engineering, University of Southern California, Los Angeles, CA, 90089, USA. [4]Norris Comprehensive Cancer Center, Keck School of Medicine, University of Southern California, Los Angeles, CA, 90033, USA. [5]USC Stem Cell, Keck School of Medicine, University of Southern California, Los Angeles, CA, 90033, USA. Correspondence and requests for materials should be addressed to K.S. (email: keyue.shen@usc.edu)

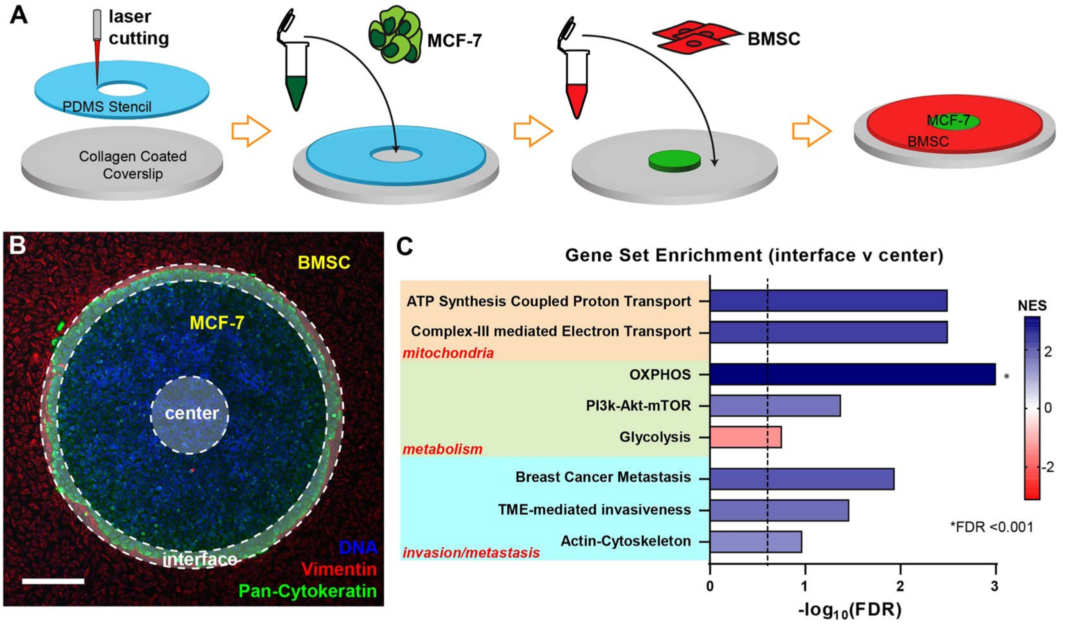

Figure 1. Spatial regulation of mitochondrial, metabolic, and metastatic pathways in micropatterned tumor-stromal assays (µTSA) assessed by RNA sequencing. (**A**) Schematics depicting the steps to create a MCF-7/BMSC µTSA; (**B**) Representative micropattern of an MCF-7 island (green: Pan-Cytokeratin) surrounded by BMSCs (red: Vimentin). Blue: nuclei. Scale bar: 100 µm. Cancer cells from the center and edge of the µTSA (opaque annular ring with dotted outlines) were isolated by laser capture microdissection[17], and their RNA was extracted and sequenced; (**C**) Gene sets found to be enriched at the interface vs. center by RNA sequencing and gene set enrichment analysis (glycolysis has negative NES indicating enrichment in the center). (See Methods for more details. FDR: False Discovery Rate; FDR < 0.25 was considered significant.) MCF-7 cells from >6 micropatterns/experiment were microdissected and combined before RNA isolation and sequencing; N = 2 independent experiments.

The tumor microenvironment (TME) plays an important role in cancer progression and metastasis[14]. The TME of progressing breast tumors is often characterized by distinct architectural and cytological features, including an evolving tissue interface of direct tumor-stromal interactions[15–18] and a stiffening tumor mass[19]. Recently, it was reported that some stromal cells can regulate metabolic and/or mitochondrial functions in cancer cells through paracrine growth factor signaling and metabolite exchange[20,21], or through transfer of mitochondrial DNA into cancer cells[3,4]. On the other hand, biomechanical properties of the TME have also been found to influence cancer cell invasiveness and metastatic potential[19,22]. At the tissue level, mechanical stresses in solid tumors are spatially dependent on tumor architecture and growth[23]. At the cellular level, mechanical cues are involved in regulating cancer cell proliferation[24], invasiveness[25], and extracellular matrix (ECM) remodeling[26,27]. Although not yet reported in cancer cells, it has been shown that mechanical stimuli can affect mitochondrial activity in cardiomyocytes and endothelial cells[28], and that cytoskeletal remodeling leads to changes in mitochondrial dynamics[29]. However, it remains unclear whether stromal cells and their associated mechanical cues within the tumor architecture can drive heterogeneous mitochondrial activities.

We have previously established a micro-engineered tumor model, i.e., a micropatterned tumor-stromal assay (µTSA), to demonstrate that tumor-stromal interactions within the architectural context of a tumor play an important role in inducing phenotypic heterogeneity in cancer and stromal cells *in vitro*, which was confirmed *in vivo*[17]. In this report, we use the µTSA to investigate the role of stromal cells in regulating tumor mitochondrial heterogeneity *in vitro*. We reveal that $\Delta\Psi_m$, mitochondrial mass, metabolism, and metastatic potential are spatially distributed within the µTSA. We show that $\Delta\Psi_m$ levels correlate with YAP/TAZ nuclear translocation status, are regulated by stromal confinement, and are dependent on the actin cytoskeleton. We further demonstrate a positive correlation between $\Delta\Psi_m$ levels and metastatic potential in cancer cells *in vivo*. We demonstrated in the µTSA a new regulatory role that the TME plays in mitochondrial heterogeneity and metastatic potential.

Results

Mitochondrial and metastatic pathways are upregulated at the tumor-stromal interface in the µTSA.

To recapitulate cell-cell interactions within the tumor architectural constraints of the TME[17], MCF-7 breast cancer cells were cultured in the µTSA with surrounding bone marrow stromal cells (BMSC)[30] (Fig. 1A), resulting in adjacent spatial compartments of cancer and stromal cells with a defined tumor-stromal interface (Fig. 1B). To examine whether cancer cell phenotypes and signaling were differentially regulated at the transcriptome level, we used laser-capture microdissection (LCM) to obtain cancer cells from the interfacial and central regions of the µTSA island, and performed RNA sequencing (RNA-seq) on these cells. The RNA-seq data were analyzed by gene set enrichment analysis (GSEA), where statistical values were generated through the Wald Test, and gene sets were ranked by statistical significance and fold change direction (see Methods). Among the pathways that differ between the interface and center, we identified three categories gene sets among the 8 that were of interest in this study (Fig. 1C), i.e., 1) mitochondrial proton/electron transport activities; 2) cellular metabolism; and 3) cancer invasion and metastasis[31–38]. Specifically, genes related to mitochondrial activities were highly dependent on the cell location in the μTSA, with cells at the interface exhibiting upregulation of the electron and proton transport genes. At the metabolic level, interfacial cancer cells had upregulation of genes involved in oxidative phosphorylation (OXPHOS), contrary to cells at the center of the micropattern that showed upregulation of glycolysis genes. Consistent with the OXPHOS upregulation, genes from the PI3K-Akt-mTOR pathway[39] were found to be upregulated at the interface. Notably, gene sets involved in actin-cytoskeleton and TME-mediated invasiveness were also upregulated at the interface, suggesting a role of the interface in cancer cell mechanics and migration. Importantly, a gene set that has been found to predict metastasis in lymph node-negative ER + breast cancer[37] was also upregulated at the interface (Fig. 1C), matching the ER + subtype of MCF-7. The results here demonstrate spatially regulated heterogeneity of gene sets for mitochondrial activities, metabolism, and metastatic potential in cancer cells in the μTSA.

Mitochondrial membrane potential ($\Delta\Psi_m$) is spatially regulated in the μTSA.

To confirm that the mitochondrial proton/electron transport pathway is upregulated in the μTSA, we stained cells with tetramethylrhodamine methyl ester (TMRM), a reversible mitochondrial membrane potential ($\Delta\Psi_m$) dye, which only accumulates in active mitochondria with intact membrane potential[40]. As shown in Fig. 2A, the $\Delta\Psi_m$ of MCF-7 cells in the μTSA had a distinct spatial profile, with lower $\Delta\Psi_m$ in cells at the center of the tumor micropattern, and higher in those closer to the interface. To validate that the TMRM signal is reflective of $\Delta\Psi_m$, we treated the micropatterns with the $\Delta\Psi_m$ uncoupler, carbonyl cyanide-4-(trifluoromethoxy)phenylhydrazone (FCCP)[41]. The FCCP treatment led to TMRM fluorescence loss in all MCF-7 cells (Fig. 2A,B). To quantitatively analyze the spatial regulation, we plotted the radial distribution of TMRM fluorescence within these micropatterns, where the normalized radial distances of 0 and 1 indicate the approximate center and edge of the micropatterned tumor island, respectively, and distances greater than 1 represent the surrounding stromal cell areas (Fig. 2B). TMRM fluorescence in MCF-7 cells within the micropattern was significantly higher than the residual TMRM fluorescence post-FCCP treatment at radial distances greater than 0.52 (as indicated by the red point on the no-treatment (NTX) curve in Fig. 2B).

Next, we investigated whether the differences in $\Delta\Psi_m$ were due to a difference in mitochondrial mass in the cells at the center and interface. On Day 4 of μTSA cell culture, we fixed and immunostained cells for TOM20, a protein expressed on the mitochondrial outer membrane and commonly utilized for mitochondrial quantification[42] (Fig. 2C). The fluorescence intensities of TOM20 and TMRM staining at the interface were both normalized against those at the center of the μTSA. We found that both mitochondrial mass and $\Delta\Psi_m$ were enhanced at the interface compared to the center, but that the enhancement in $\Delta\Psi_m$ (~3.1 fold) was significantly higher than that of the mitochondrial mass (~1.7 fold) (Fig. 2D). The results indicate that the ΔΨm increase at the interface is mainly due to increased proton gradient, and not to increased mitochondrial mass.

Fluorescence microscopy of metabolic coenzymes reveals enhanced redox activity at the interface.

To examine the differential metabolic functions in the μTSA, we employed a non-invasive, label-free approach, using microscopic imaging of the naturally occurring auto-fluorescence of the metabolic coenzymes, nicotinamide adenine dinucleotide (NADH) and its phosphate ester NADPH, designated NAD(P)H as their fluorescence cannot be distinguished[43,44] (Fig. 3A,B), as well as flavin adenine dinucleotide (FAD) (Fig. 3C,D). The fluorescence of FAD and NAD(P)H was simultaneously acquired through 540/50 nm and 460/80 nm emission filters with a single two-photon excitation laser light source at 780 nm. The fluorescence signals were then processed to obtain the optical redox ratio (ORR), which is indicative of OXPHOS metabolism[45], and is defined as the ratio of FAD fluorescence over the sum of signal intensity from FAD and NAD(P)H (Fig. 3E). The images were further segmented based on FAD intensity for mitochondrial regions[46] at the subcellular level to specifically measure the ORR in mitochondria in individual cells (Fig. 3F). We observed altered energy metabolism in the mitochondria of interfacial cancer cells indicated by their higher ORR when compared to cells at the center of the μTSA (Fig. 3F). The results are consistent with the RNA-seq data showing spatially elevated mitochondrial OXPHOS at the μTSA tumor-stromal interface.

$\Delta\Psi_m$ spatial profile correlates with YAP/TAZ nuclear localization in the micropatterns.

We then aimed to investigate the basis for the spatial differences in $\Delta\Psi_m$ within the micropatterns. We had observed a significant upregulation of actin-cytoskeleton related genes at the tumor-stromal interface (Fig. 1C), which led us to hypothesize that the spatial patterns of $\Delta\Psi_m$ in the μTSA result from the differential cellular constraints experienced by the epithelial cancer cells within the tumor island. Cells at the interface are weakly confined by stromal cells, whereas those closer to the center undergo heavier constraints from the neighboring epithelial cells. To test this hypothesis, in addition to the regular MCF-7-BMSC μTSA, we micropatterned MCF-7 islands surrounded by a thin layer of micro-contact printed polydimethylsiloxane (PDMS) to impose complete physical constraints on the island, as well as MCF-7 islands without stromal cells or PDMS, which lack epithelial or stromal constraints (Fig. 4A). Using TMRM staining, we found distinct differences in the spatial distribution of $\Delta\Psi_m$ within the MCF-7 islands in the three micropatterns (Fig. 4B). MCF-7-BMSC μTSA showed higher $\Delta\Psi_m$ in MCF-7 cells closer to the interface, consistent with results in Fig. 2. Constraining the tumor island with PDMS led to an almost complete loss of high $\Delta\Psi_m$ at the micropattern edge. However, when the micropatterned tumor island grew free of any physical constraints, a wider band of cells with high $\Delta\Psi_m$ was observed at the periphery of the micropattern (Fig. 4B).

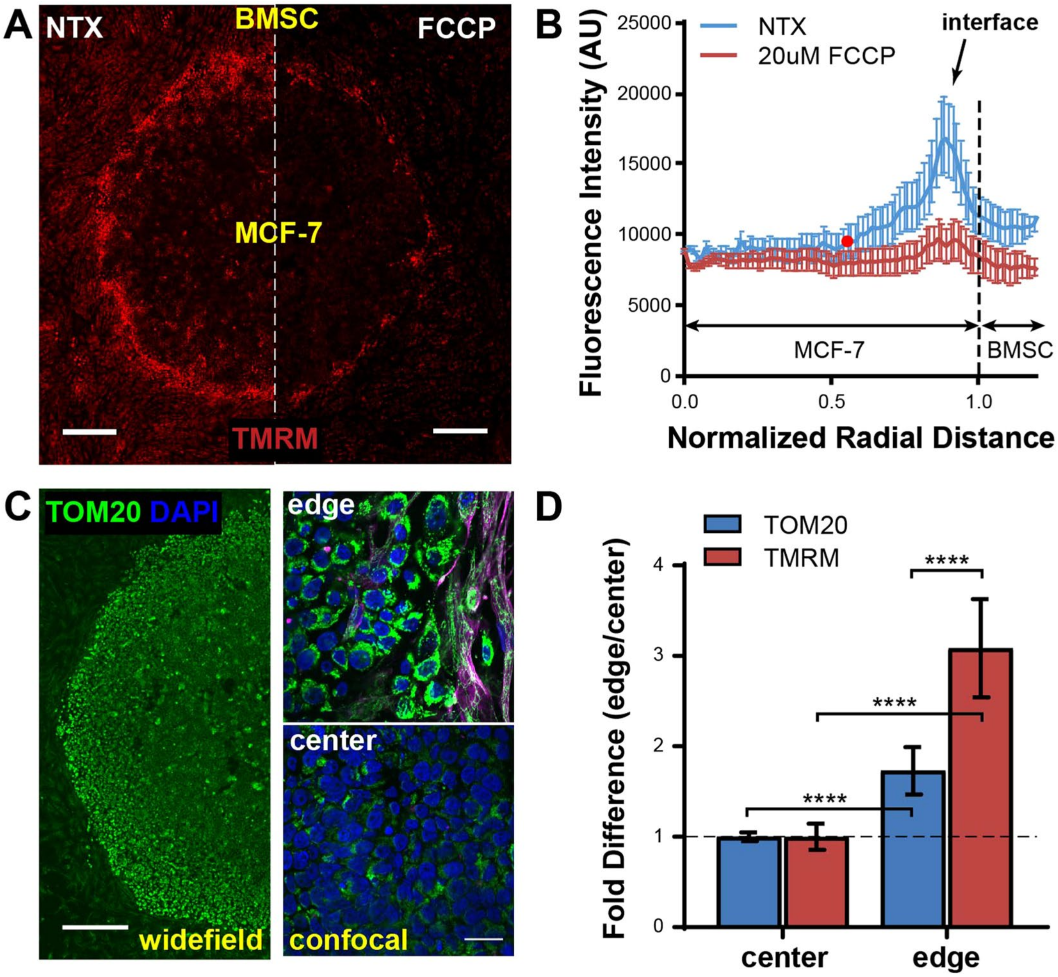

Figure 2. Differential regulation of mitochondrial membrane potential ($\Delta\Psi_m$) and mass at the interface vs. center in the μTSA. (**A**) $\Delta\Psi_m$ levels assessed by TMRM fluorescence on Day 4 MCF-7-BMSC μTSA before and after addition of 20 μM FCCP uncoupler. Scale bar: 500 μm; (**B**) Representative radial distribution of TMRM fluorescence in a MCF-7-BMSC μTSA on day 4 before and after FCCP treatment. The red dot ($r = 0.52$) on the no-treatment (NTX) curve indicates that the TMRM fluorescence to the right of the dot is significantly higher than that of all FCCP-treated samples; from N = 6 independent experiments ($p < 0.05$, Welch's t-test); (**C**) μTSA stained for mitochondrial mass with anti-TOM20. Right panels: confocal scans of the edge and the center. Green: TOM20; purple: vimentin; blue: DAPI. Scale bars: 500μm in widefield (left) and 25μm in confocal (right). (**D**) Fold difference in TMRM and TOM20 fluorescence between the edge and the center. N = 3 independent experiments. P-values: ordinary one-way ANOVA.

To get a better molecular understanding of the $\Delta\Psi_m$ regulation, we immunostained the micropatterns for the transcriptional regulators, YAP/TAZ, which can translocate from the cytosol to the nucleus, reflecting contact-mediated Hippo-signaling[47,48] or mechanical cues experienced by the cells[49,50]. Figure 4B shows representative images of subcellular localization of YAP/TAZ at the center and edge of the micropatterns. The percentage of cells with nuclear YAP/TAZ in these regions was calculated (Fig. 4C). We found that MCF-7 cells at the edges of the co-culture or of the monoculture had higher levels of nuclear YAP/TAZ when compared to their respective centers. When surrounded by PDMS, YAP/TAZ localization across the whole micropattern became predominantly cytoplasmic, as seen at the center of the mono- and co-cultures (Fig. 4B,C). Interestingly, the percentage of nuclear YAP/TAZ in MCF-7 cells at the edge of co-cultures was intermediate and significantly different from those at the edges of the monoculture and PDMS-confined controls, suggesting that stromal cells impose an intermediate level of physical constraints. Next, we plotted nuclear YAP/TAZ vs. TMRM fluorescence from the monoculture and co-culture conditions. We picked three locations (edge, center, and intermediate) from the monoculture and two locations (edge and center) from the co-culture based on the visible differences in TMRM intensities among these regions. Interestingly, we found a strong positive correlation between the two parameters ($p = 0.032$, $R^2 = 0.8279$, Fig. 4D). Together, the results suggest that the spatial distribution of $\Delta\Psi_m$ of cancer cells in micropatterns stems from the differential physical constraints imposed on cells.

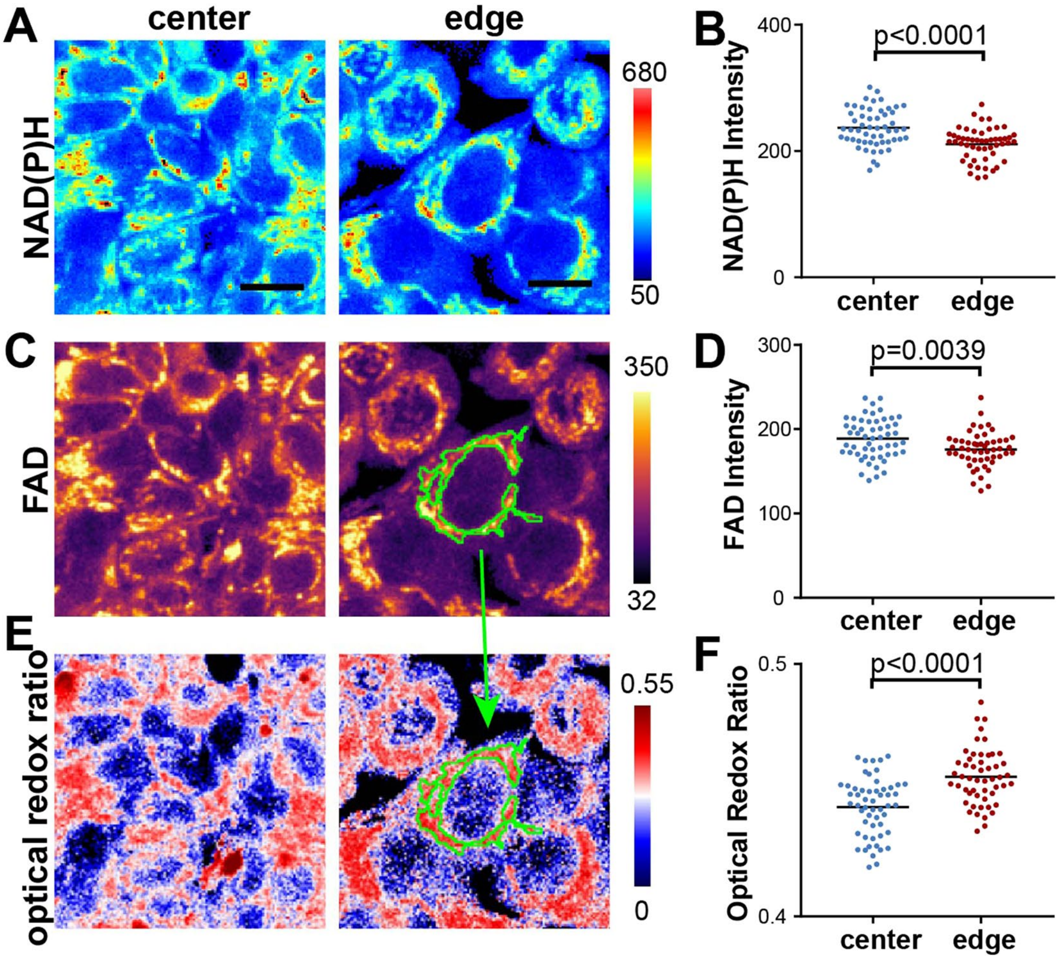

Figure 3. Redox imaging of cancer cells in a μTSA. Representative images of (**A**) NAD(P)H fluorescence; (**C**) FAD fluorescence; and (**E**) optical redox ratio (defined as FAD/(FAD + NAD(P)H)) at the center and edge of the μTSA on day 4. Scale bar: 25 μm. Quantification of (**B**) NAD(P)H and (**D**) FAD fluorescence intensities, and (**F**) the optical redox ratio at the single-cell level from the center (blue dots) or the edge (red dots) areas within the μTSA. Mitochondrial regions are segmented from FAD images and applied to the optical redox ratio images (green regions in **C**,**E**). Color scale is to the right of each image. (Representative dataset from N = 4 independent experiments; p-values: Welch's t-test.)

$\Delta\Psi_m$ distribution and YAP/TAZ nuclear translocation in μTSA are modulated by stromal density. We noticed that the width of the cancer cell region with high $\Delta\Psi_m$ at the tumor-stromal interface of the μTSA co-culture was variable within the same micropattern, as illustrated in Fig. 4B. A similar non-uniformity was also seen with nuclear translocation of YAP/TAZ in these co-cultures, as evidenced by the large standard deviation in Fig. 4C. As YAP/TAZ is involved in contact-mediated growth regulation, we hypothesized that these variations may be due to differences in local cancer cell densities as a result of differential stromal constraints. To test this hypothesis, we investigated whether the $\Delta\Psi_m$ profile, YAP/TAZ nuclear translocation, and interfacial cancer cell density could be altered by the initial seeding density of the stromal cells. MCF-7 cells were micropatterned with three stromal densities (221, 442 or 884 cells/mm^2, corresponding to 25k, 50k, and 100k initial seeding numbers in Fig. 5A–C), and stained for $\Delta\Psi_m$ with TMRM and YAP/TAZ by immunostaining on day 4. Consistent with our hypothesis, we found that the interfacial region of cancer cells with high $\Delta\Psi_m$ was much wider in the micropatterns with a lower stromal density than in those with higher densities (Fig. 5A). As controls, the open-edge and PDMS-confined mono-cultures showed the widest and narrowest regions of cancer cells with high $\Delta\Psi_m$, consistent with those in Fig. 4. To quantitatively compare the $\Delta\Psi_m$ profiles, we analyzed the radial distribution of TMRM fluorescence in the micropatterns. In the open-edge micropatterns, the cancer cell region with high $\Delta\Psi_m$ was wide, with $\Delta\Psi_m$ peaking rapidly at a normalized radial distance as low as 0.67 (the edge is at $r = 1$). In the μTSA co-cultures, however, the width of the high $\Delta\Psi_m$ region was narrower and the peak closer to the interface ($r = 0.85, 0.91, 0.92$ as stromal cell seeding density increased) (Fig. 5B). In the PDMS-confined micropatterns, $\Delta\Psi_m$ was uniformly low throughout the tumor island, except at the very edge, where cells clump along the PDMS barrier, leading to a slight increase in observed TMRM fluorescence. Strikingly, YAP/TAZ nuclear localization followed a similar trend as the $\Delta\Psi_m$. The increased stromal density led to lower nuclear YAP/TAZ in the interfacial cancer cells (Fig. 5C). Noticeably, under the initial stromal density of 50k per well (442 cells/mm^2), interfacial

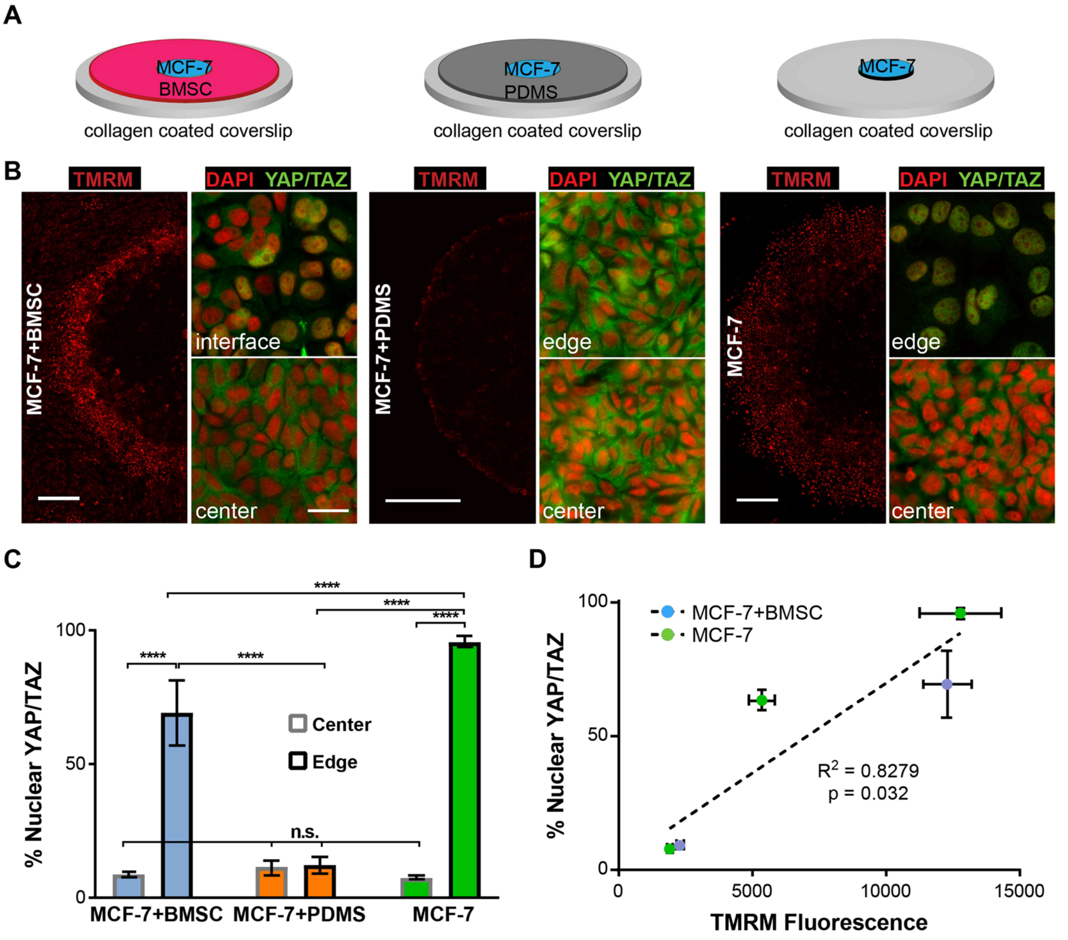

Figure 4. Correlation of $\Delta\Psi_m$ and YAP/TAZ nuclear translocation in micropatterns. (**A**) Schematics of the three micropattern cultures used in this experiment; (**B**) TMRM staining of $\Delta\Psi_m$ (scale bar: 500 μm) and YAP/TAZ immunostaining (scale bar: 25 μm) in the three micropatterns on day 4; (**C**) Quantification of cancer cells with nuclear YAP/TAZ localization at the center and edge of the μTSA (n.s.: not significant; $****p < 0.0001$ by ordinary one-way ANOVA); Representative dataset from N = 3 independent experiments. (**D**) Linear regression of YAP/TAZ nuclear localization and TMRM fluorescence in cancer cells in the monoculture and co-culture μTSA. Three locations (center, edge and approximately 700 μm away from the edge) were taken from the monoculture μTSA and two locations (center and edge) from the co-culture. (Representative dataset, N = 2 independent experiments; p-value: zero-slope hypothesis in linear regression).

cancer cells still had significantly higher nuclear YAP/TAZ than those in the center. However, such difference was abrogated with higher stromal seeding density. Cells at the center of all the micropatterns showed a uniformly low nuclear YAP/TAZ localization (Fig. 5C).

Next, we quantitatively analyzed the impact of stromal densities on cancer cell growth and size, and their relationship with the $\Delta\Psi_m$ profile. While cancer cells are generally considered not to be subjected to growth arrest from contact inhibition[51], in our μTSA model, the area of the tumor island with higher stromal density appeared smaller than those seeded with lower stromal density (Fig. 5A,D), suggesting growth retardation and/or size restriction due to the physical constraints imposed by stromal cells. To simplify the analysis, we initially modeled cell growth in the micropatterns by measuring the size of the tumor islands. Cell growth is typically described as an exponential model, $Y = Y_0 e^{kt}$, where Y_0 is the initial population size, k is the growth rate, and t is the growth time[52]. To incorporate the impact of stromal density, we modified the growth curve to:

$$Y = Y_0 e^{k(s)t} \tag{1}$$

where $k(s)$ becomes a function of stromal density s. Interestingly, using curve fitting, we found a simple relationship of exponential decay between Y and s ($R^2 = 0.9599$) (Fig. 5D). With growth time t being a fixed value (Day 4), the result implies that $k(s)$ is a linear function of s with a negative slope:

$$k(s) = -k's \tag{2}$$

Here, k' is a rate constant representing the growth restricting effect from the stromal confinement. Interestingly, we found that the area of cancer cells with high $\Delta\Psi_m$ (normalized by the total area of the tumor island) also had a

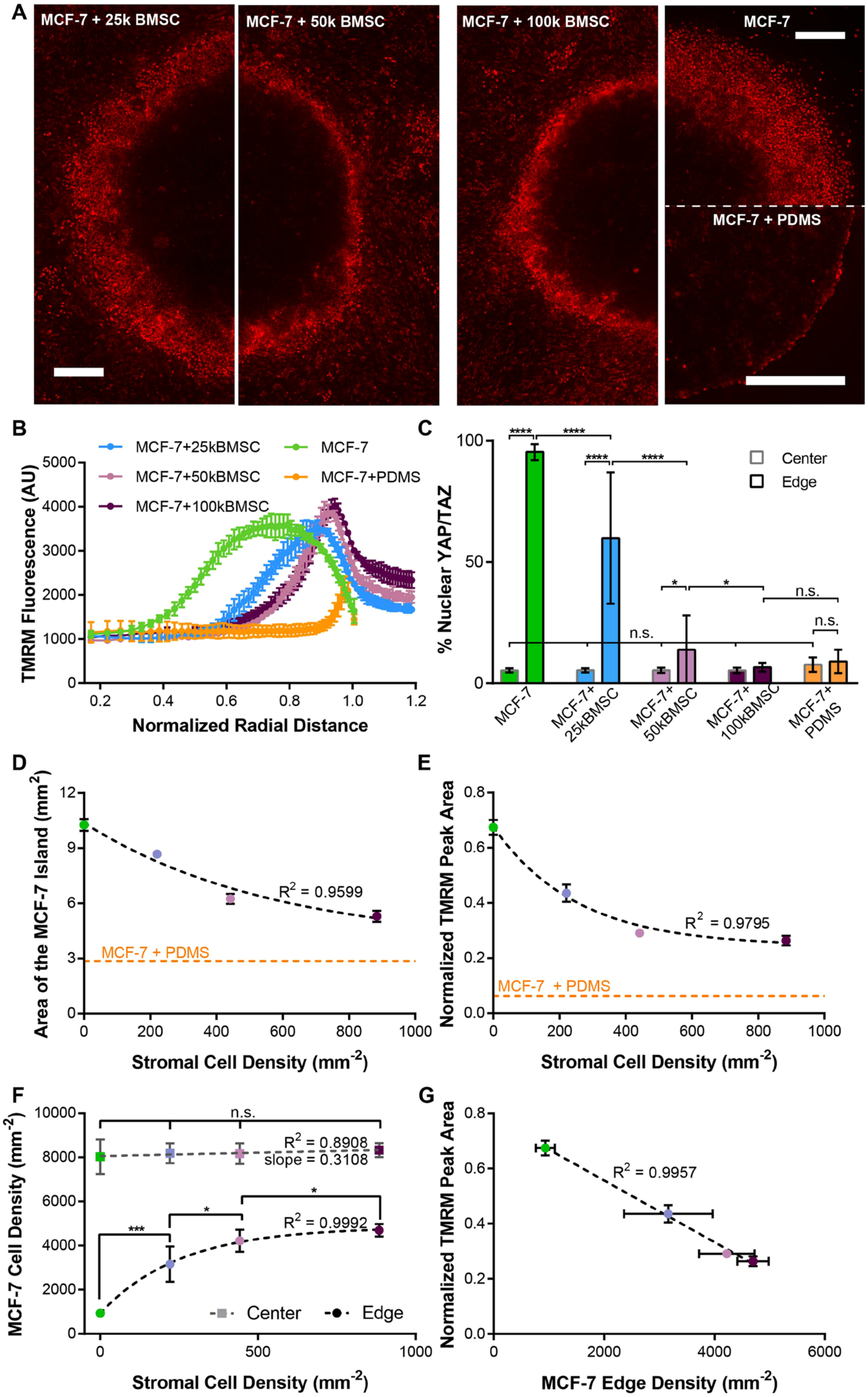

Figure 5. Regulation of cancer cell $\Delta\Psi_m$ by stromal density. (**A**) TMRM fluorescence in a μTSA with BMSC seeding densities varying from 25,000, 50,000, to 100,000 cells per micropattern. Monocultures without or with PDMS constraint were used as controls. Scale bars: 500 μm; (**B**) Normalized radial distribution of TMRM fluorescence in micropatterns; (**C**) Percentage of YAP/TAZ nuclear localization in cancer cells at the edge and center of the micropatterns (n.s.: not significant, $^*p < 0.05$, $^{****}p < 0.0001$ by ordinary one-way ANOVA); (**D**) Areas of cancer islands as a function of the initial stromal density on Day 4. Non-liner regression: single-exponential decay; (**E**) TMRM peak area at the interface normalized to total cancer area of the respective micropattern as a function of initial stromal density. Non-linear regression: single-exponential decay; (**F**) Cancer cell densities at the center (red curve) and edge (black curve) of micropatterns. ($^*p < 0.05$, $^{***}p < 0.001$, by Kruskal-Wallis test); (**G**) Normalized TMRM peak area as a linear function of cancer cell density at the interface. Linear regression $R^2 = 0.9957$. Representative dataset shown from N = 3 independent experiments for MCF-7, MCF-7 + 50k BMSC, and MCF-7 + PDMS micro-patterns, N = 1 for MCF-7 + 25k BMSC and MCF-7 + 100k BMSC micropatterns.

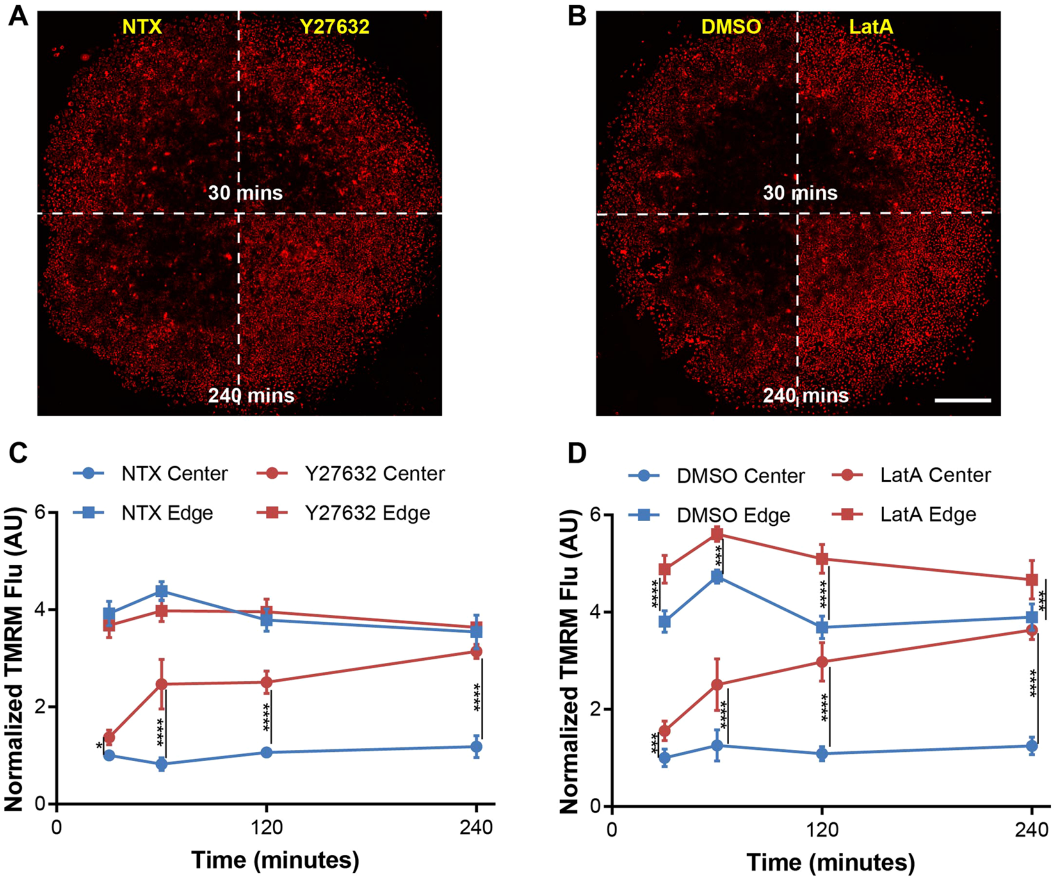

Figure 6. Loss of $\Delta\Psi_m$ heterogeneity by inhibition of mechanotransduction. (**A**,**B**) TMRM fluorescence in monoculture μTSA on day 4 treated with inhibitors of mechanotransduction: Y-27632 (50 μM, ROCK inhibitor) and Latrunculin A (LatA, 0.5 μM, actin polymerization inhibitor) from 30 to 240 minutes. Scale bar: 500 μm; (**C**,**D**) Changes of TMRM fluorescence in cancer cells at the center and edge as a function of treatment time (Representative dataset from $N = 3$ independent experiments; $^*p < 0.05$, $^{***}p < 0.001$, $^{****}p < 0.0001$, by ordinary one-way ANOVA).

similar relationship with stromal density, with a high coefficient of determination ($R^2 = 0.9865$) (Fig. 5E), suggesting a direct role of physical confinement on $\Delta\Psi_m$ distribution. We further investigated whether such regulation is mediated through the cancer cell size at the tumor-stromal interface. We plotted cancer cell densities at the center and interface of the μTSA against the initial stromal seeding densities. Indeed, higher stromal seeding density correlated with higher cancer cell density (thus smaller cancer cell sizes) at the edges of the micropatterns (Fig. 5F). Lastly, a strong negative correlation existed between the density of cancer cells and the normalized area of cancer cells with high $\Delta\Psi_m$ (Fig. 5G). These results suggest that stromal confinement controls the spatial distribution of $\Delta\Psi_m$ in cancer cells by regulating their growth and size.

Inhibiting the Rho-associated protein kinase and actin polymerization leads to a loss of $\Delta\Psi_m$ spatial distribution. Rho-associated protein kinase (ROCK) and the actin cytoskeleton are upstream of YAP/TAZ and are intricately involved in both contact-mediated Hippo-YAP signaling and contact-independent mechano-signaling through YAP/TAZ[49,53]. To investigate the involvement of ROCK and actin cytoskeleton in the spatial distribution of $\Delta\Psi_m$, we used two chemical inhibitors, Y-27632 and Latrunculin A (LatA), both of which relax cellular actin tension and inhibit mechanotransduction[54,55], and the open-edge monoculture (Fig. 4A, right), which eliminates the potential influence of stromal factors other than the physical confinement, while retaining the spatial distribution of $\Delta\Psi_m$ (Fig. 4B, right). LatA directly inhibits actin polymerization, and Y-27632 decreases actin tension by phosphorylating myosin light chain and activating myosin II[56]. Both Y-27632 and LatA inhibited regular actin polymerization in MCF-7 cells at the center and edge of the micropatterns (Supplementary Fig. S1). At the center of the micropatterns, the MCF-7 cells originally had actin localization at the cell junctions, which became discontinuous upon treatment with Y-27632 and LatA. At the edge of the micropattern, those treated with Y27632 acquired thin lamellar extensions and showed a decrease in actin stress fibers, while those treated with LatA demonstrated an increased abundance of punctate actin clusters (Supplementary Fig. S1), as reported elsewhere[50,57].

As shown in Fig. 6A,B, both Y-27632 and LatA increased the $\Delta\Psi_m$ (TMRM) in the cancer cells at the center of the micropatterns over a 4-hour period. The increase started as early as 30 min after treatment, rose rapidly between 30 min and 1 hour, and became slower from 1 to 4 hours (Fig. 6C,D). Notably, the two drugs had distinct

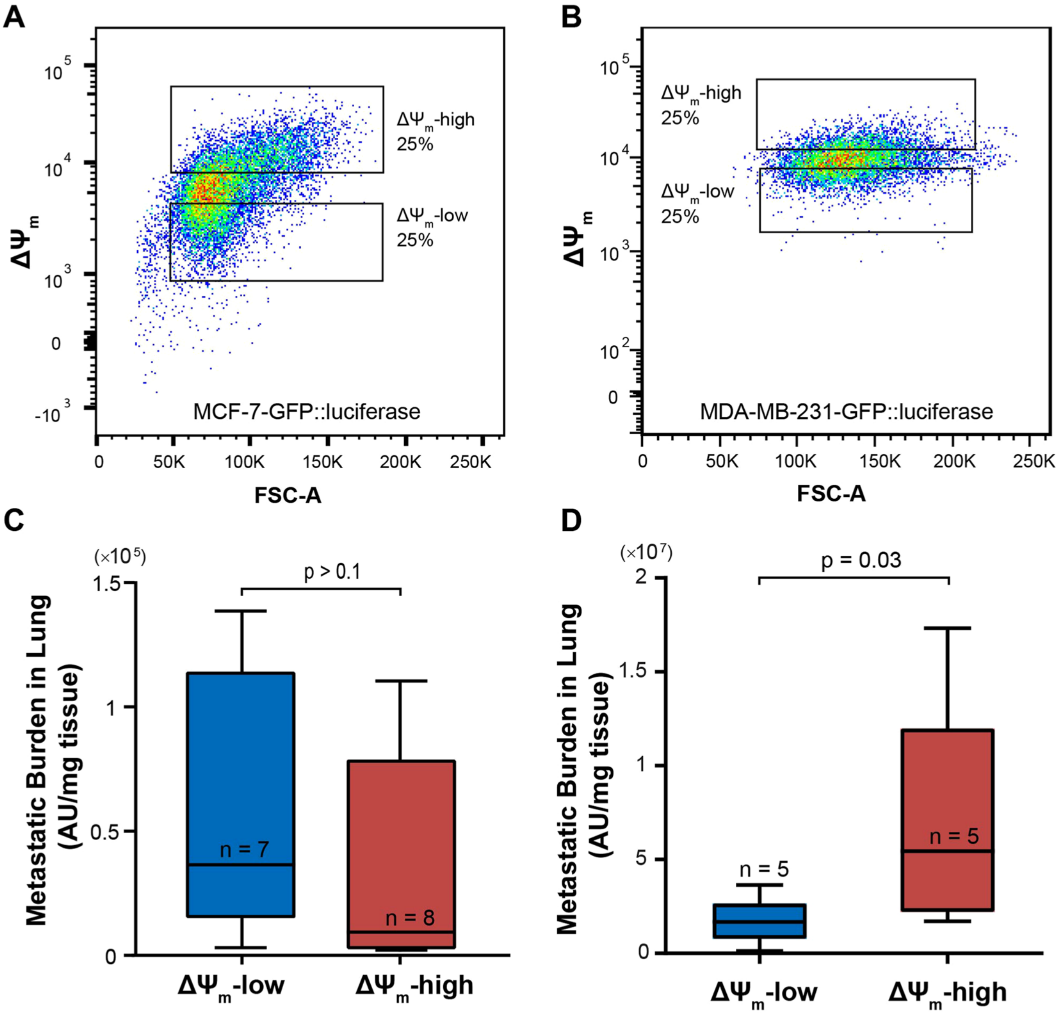

Figure 7. Correlation of $\Delta\Psi_m$ with metastatic potential in vivo. (**A**) MCF-7 cells and (**B**) MDA-MB-231 cells, both transduced with GFP/luciferase, were sorted into a $\Delta\Psi_m$-high and -low subpopulations for tail-vein injection into NSG mice; Quantification of the metastatic burden in the lungs of mice injected with (**C**) MCF-7 cells at week 5 and (**D**) MDA-MB-231 cells at week 4, via *ex vivo* quantification of luciferase activity in tissue lysate (p-values: Mann-Whitney test).

effects on cancer cells. Y-27632 increased the $\Delta\Psi_m$ only at the center of the micropatterns (Fig. 6C), while LatA treatment significantly enhanced the $\Delta\Psi_m$ both at the edge and center of the micropatterns at all the time points (Fig. 6D). These results demonstrate a dependence of $\Delta\Psi_m$ regulation on actin cytoskeleton[58] and Rho-ROCK signaling[59], and on cell location within the micropatterns.

$\Delta\Psi_m$ level correlates with metastatic potential *in vivo*. We next sought to investigate the *in vivo* significance of the $\Delta\Psi_m$ heterogeneity. RNA-seq data suggested that cancer cells at the tumor-stromal interface have higher $\Delta\Psi_m$ and elevated expression of a gene set related to metastasis (Fig. 1C). MCF-7 cells are known to be weakly metastatic[60,61]. Therefore, we used both MCF-7 and MDA-MB-231 cells, the latter of which is a metastatic breast cancer cell line, to determine if any correlation exists between $\Delta\Psi_m$ and metastatic potential *in vivo*. MCF-7 and MDA-MB-231 cells were sorted into subpopulations with high and low-$\Delta\Psi_m$ (top and bottom 25%, Fig. 7A,B), and then separately inoculated through tail vein injections into immune-deficient NSG (NOD.Cg-*Prkdc*^{scid} *Il2rg*^{tm1Wjl}*/SzJ*) mice (the mice for MCF-7 cells were pre-implanted with estrogen pellets; see Methods). Both MCF-7 and MDA-MB-231 cells had been previously transduced with a GFP/firefly luciferase-reporter construct for downstream *ex vivo* measurement[62,63]. Metastases were allowed to develop for four (for MDA-MB-231) or five (for MCF-7) weeks post injection. At the end, mice were sacrificed, their lungs were snap-frozen, crushed, and lysed, and the luciferase signal per tissue weight was measured to assess metastatic burden[17]. In mice injected with MCF-7 cells, the luciferase signal from the lung tissues was low compared to those with MDA-MB-231 cells (Fig. 7C,D), and there was no significant difference between the lung metastatic burden between mice injected with $\Delta\Psi_m$-high and those with $\Delta\Psi_m$-low MCF-7 cells (Fig. 7C). Strikingly, while MDA-MB-231 cells are known to be highly aggressive, and had a tighter distribution of $\Delta\Psi_m$ than MCF-7 cells (Fig. 7B), mice injected with the $\Delta\Psi_m$-high MDA-MB-231 cells had a significantly higher metastatic burden than those injected with $\Delta\Psi_m$-low cells ($p = 0.03$, Mann-Whitney test, Fig. 7D).

Discussion

TME-mediated metabolic reprogramming plays an important role in sustaining tumor growth and progression[8,21,64–70]. In this study, by using a micropatterned co-culture model mimicking the morphological features of early breast tumors[17,18], we show that mitochondrial and metabolic phenotypes can be spatially regulated by surrounding stromal cells under the architectural context of tumor-stromal interactions. Specifically, mitochondrial mass, $\Delta\Psi_m$ and optical redox ratio (ORR) are enhanced near the tumor-stromal interface as compared to the center of the tumor nest. Importantly, $\Delta\Psi_m$, a mitochondrial feature previously linked to cancer invasiveness[10], is directly controlled by the physical confinement imposed by the surrounding stromal cells, which correlates with YAP/TAZ nuclear localization. We further demonstrated that the spatial regulation of $\Delta\Psi_m$ by physical confinement is dependent on ROCK signaling and actin polymerization, and that high $\Delta\Psi_m$ correlates with increased metastatic potential *in vivo*. To the best of our knowledge, such relationships have not been previously reported in cancer cells. Our results suggest that cancer cells can perceive physical cues from stromal cells, which may potentially regulate their metastatic behavior. As this study was done with breast cancer cells, more studies are needed to further examine the signaling pathways underlying the physical regulation of mitochondrial heterogeneity, and determine the applicability of these findings to other cancer and stromal cell types. Notably, some other physical cues within the TME, such as oxygen gradients and ECM stiffness, are also tightly associated with the tumor architecture[71,72] in early cancer progression, and have been shown to alter cancer cell metabolism[73–75]. Additional studies are envisioned to elucidate the contribution of these components to the heterogeneous mitochondrial phenotypes.

In the current study, we uncovered that physical confinement from stromal cells controls the local density/size of the cancer cells and their $\Delta\Psi_m$ level (Fig. 5). Interestingly, it has been reported that mitochondrial content/mass scales linearly with cell size in HeLa cells[76], human umbilical vein endothelial cells (HUVECs)[77], and budding yeast[78]. More recently, Miettinen and Bjorklund showed that $\Delta\Psi_m$ and OXPHOS follow a non-linear, bell-shaped relationship with cell size, and those with an 'optimal' cell size at the highest $\Delta\Psi_m$ seem to have decreased apoptosis and enhanced cellular proliferation[77]. Our observed co-upregulation of mitochondrial mass, $\Delta\Psi_m$ and OXPHOS in the μTSA thus support the cell size theory and suggest a survival/proliferative advantage of the interfacial cancer cells in the μTSA. More intriguingly, our study further revealed an adaptive response of cancer cell size and $\Delta\Psi_m$ to the physical confinement by stromal cells in TME. As stromal density increases, the density of cancer cells at the interface becomes higher; however, it plateaus at a density that is still much lower than that at the center of the micropattern (Fig. 5F). Nevertheless, while the width of the interfacial cancer cell region with higher $\Delta\Psi_m$ becomes narrower with higher stromal density, the peak fluorescence intensity of the $\Delta\Psi_m$ staining remains similar across all the patterns (except the PDMS confined culture). These results suggest that the cancer cells near the tumor-stromal interface can accommodate and adjust their sizes to retain an 'optimal' mitochondrial state/functionality, which is absent in the PDMS-confined culture.

In this study, we also observed preferential localization of YAP/TAZ in the cytoplasm or nuclei of cells at the center or interface of μTSA, respectively. This observation is in agreement with previous findings on YAP/TAZ regulation by cell density[53]. Importantly, at the population level, we further revealed a linear correlation between $\Delta\Psi_m$ and YAP/TAZ nuclear translocation in the micropatterns (Fig. 4D). It is unclear, however, whether this represents a causal relationship. It has been shown that YAP overexpression in breast cancer cells leads to increased mitochondrial mass[79]. On the other hand, PLD6-mediated increase in mitochondrial fusion was shown to inhibit YAP/TAZ activity through AMPK-mediated YAP/TAZ phosphorylation in human mammary epithelial cells[80]. These studies and ours suggest a crosstalk between mitochondrial dynamics and YAP/TAZ activation. Additional studies are needed to further elucidate the signaling relationship between $\Delta\Psi_m$ and YAP/TAZ.

It is noteworthy that nuclear YAP/TAZ have been found to act as relays of mechanical signals resulting from cell density[53], ECM stiffness[49], and intracellular cytoskeletal tension[56]. Recent studies have shown mitochondrial functions to be actin-dependent. Mitochondrial fusion and fission rely on dynamic actin polymerization[29]. $\Delta\Psi_m$ cannot be maintained in mouse embryonic fibroblasts when β-actin is knocked out[81]. On the other hand, Furukawa *et al.* have recently shown that the cell density dependence of YAP/TAZ localization is mediated through intracellular actin tension[56]. Cellular actin tension was reduced in the micropatterns using LatA and Y-27632. The distinct changes in cell morphology and actin localization upon treatment with LatA and Y-27632 were consistent with previously reported results[50,57]. On the other hand, LatA and Y-27632 treatments did not lead to differences in nuclear YAP/TAZ, even after increasing treatment time to 12 hours (Supplementary Fig. S2). The lack of response of YAP/TAZ localization to both drugs is consistent with a previous report that the dependence of YAP/TAZ localization on F-actin integrity occurs only in the absence of cell-cell contacts, but not with confluent epithelial cells[50]. Both these drugs led to an increase in cellular $\Delta\Psi_m$ in cancer cells at the center of the micropatterns (Fig. 6), confirming actin stress polymerization is upstream of $\Delta\Psi_m$ regulation. Interestingly, at the edge of micropatterns, LatA treatment increased $\Delta\Psi_m$ while Y-27632 has no effect, indicating a difference in the $\Delta\Psi_m$ regulation in cancer cells between the edge and center of the micropattern. A possible explanation is the difference in the activation of YAP signaling in these two regions. Activated nuclear YAP has been shown to negatively regulate Rho[82,83], and Rho activity is required to activate ROCK through its Rho-binding domain[84]. The difference in YAP/TAZ nuclear translocation between the two spatial regions could thus explain the difference in sensitivity to ROCK inhibition. The differential outcome with inhibition of cytoskeletal tension also suggests that cancer cells may experience different mechanical stresses (tensile vs. compressive) at the interface and center of the μTSA, which have been shown to associate with tumor architecture in a growing tumor mass[23]. Future studies aiming at measuring the distribution of stresses in the μTSA are envisioned.

Importantly, while our study points to the physical confinement imposed by the stromal cells as the main source of spatial $\Delta\Psi_m$ distribution, it does not rule out other mechanisms that may also regulate mitochondrial functions, such as biochemical signaling through cell-cell adhesion and soluble factors. One such indication comes from the fact that the interfacial cancer cells under high stromal density do not behave as the

PDMS-confined cancer cells (Fig. 5A,B). Interestingly, at the highest stromal seeding density (100k), YAP/TAZ was located in the cytoplasm both at the tumor-stromal interface and at the center (Fig. 5C); however, under the same conditions, the tumor-stromal interface still retains a thin layer of cancer cells with high $\Delta\Psi_m$. One potential mechanism of this interface-bulk difference is the metabolic interactions between tumor and stromal cells, as well as between tumor cells from different micropattern regions. For instance, both cancer-associated fibroblasts (CAFs)[85] and hypoxic tumor cells[86] have been shown to undergo glycolysis and to supply lactate to fuel cancer cells that engage in mitochondrial OXPHOS. Notably, while there is no apparent hypoxia in the µTSA, cancer cells in the center have upregulated glycolytic gene expression compared to the interfacial cells (Fig. 1C). Another potential mechanism is through heterotypic tumor-stromal adhesion or cancer-ECM interactions at the epithelial-stromal interface. For example, breast cancer cells stimulate CCL5 production from BMSCs upon tumor-stromal contact[30], which increases glucose uptake and ATP production in breast cancer cells[87]. Breast cancer cells can also secrete growth factors to activate nearby stromal cells[88], which remodel the physical and biochemical properties of the surrounding ECM through matrix metalloproteinases[89] and production of collagen[90,91]. Future studies are needed to determine the exact contributions of these biochemical factors to the heterogeneous mitochondrial phenotypes in µTSA.

While previous studies have reported association of high $\Delta\Psi_m$ in cancer cells with increased secretion of vascular endothelial growth factor (VEGF) and matrix metalloproteinase-7 (MMP-7) as well as enhanced invasiveness *in vitro*[10], the *in vivo* significance of $\Delta\Psi_m$ in cancer metastasis remained unclear. Our RNA-seq data suggested increased expression of metastasis related genes in interfacial cancer cells (Fig. 1C), leading us to hypothesize that the $\Delta\Psi_m$ of breast cancer cells is associated with their *in vivo* metastatic potential. One of the challenges of testing this hypothesis is that the MCF-7 breast cancer cells are only weakly metastatic *in vivo*[60,61] and MCF-7 mouse models are generally considered to model early-stage breast cancer[92]. We inoculated mice with MCF-7 cells sorted based on their $\Delta\Psi_m$ and assayed the lungs for metastatic burden five weeks post injections. Not surprisingly, the lung metastatic burden with MCF-7 cells was low despite of the higher inoculation doses than the MDA-MB-231 injection group. This is in accordance with a previous report which showed that MCF-7 cells injected through tail vein injection only resulted in scattered cancer cell presence in the lungs even after nine weeks, as opposed to large multicellular lung metastases in those injected with MDA-MB-231 cells in just two weeks post injection[61]. Further, we observed no difference in the lung metastatic burden between the groups injected with $\Delta\Psi_m$ -high vs. $\Delta\Psi_m$ -low MCF-7 cells (Fig. 7C), which could have resulted from the overall low metastasis forming ability of the MCF-7 cells. In stark contrast, we found that high $\Delta\Psi_m$ MDA-MB-231 cells, when injected into mice, formed significantly more lung metastases than those injected with low $\Delta\Psi_m$ cells. Together, these results suggest that while the $\Delta\Psi_m$ may not be sufficient by itself to promote metastasis, it contributes to the metastasis formation in later stage cancer progression (as supported by the MDA-MB-231 metastasis model).

Some mitochondrial activities have been previously shown to be involved in the process of breast cancer metastasis *in vivo*. PGC1-α, a master regulator of mitochondrial biogenesis, was found to be essential for lung metastasis formation in mice[13]. We demonstrated, for the first time, that breast cancer cells (MDA-MB-231) with higher $\Delta\Psi_m$ have greater metastatic potential *in vivo* (Fig. 7), which underscores the importance of investigating TME-mediated mechanisms governing mitochondrial heterogeneity. Further studies are also necessary to elucidate the relationship between mitochondrial biogenesis and $\Delta\Psi_m$, and the regulatory role of $\Delta\Psi_m$ in metastatic cascades, such as persistence in circulation, extravasation, and survival at the metastatic sites.

In summary, we have shown the impact of tumor-stromal interactions in inducing spatial heterogeneity of mitochondrial activities in the TME, with implications on the metastatic potential of cancer cells *in vivo*. We demonstrated that the differential $\Delta\Psi_m$ of cancer cells is mainly controlled by physical confinement from stromal cells, correlates with YAP/TAZ nuclear translocation, and is mediated through the actin cytoskeleton. Our study provides new insights into the role of TME in the regulation of mitochondrial heterogeneity and cancer metastasis.

Materials and Methods

Cells. MCF-7 and MDA-MB-231 cells (ATCC) were cultured in Dulbecco's Modified Eagle Medium (DMEM; Life Technologies) supplemented with 10% Fetal Bovine Serum (FBS; EMD Millipore), and 100 U/ml penicillin and 100 µg/ml streptomycin (Life Technologies). Primary human bone marrow stromal cells (BMSCs) derived from whole human bone marrow aspirates (Lonza)[93] were expanded using the MesenCult Proliferation Kit (Stem Cell Technologies). µTSA co-cultures were carried out in the FBS and penicillin/streptomycin supplemented DMEM.

Antibodies. The following primary antibodies were used in this study: TOM20 (Santa Cruz Biotechnology, sc-17764, 1:50), YAP/TAZ (Cell Signaling, rabbit mAb 8418, 1:200), pan-keratin (Cell Signaling, C11 mouse mAb 4545, 1:500), and vimentin (Cell Signaling, rabbit mAb 5741, 1:200). Alexa Fluor-conjugated secondary antibodies (Life Technologies) were used at a dilution of 1:500.

Micropatterned Tumor-Stromal Assay (µTSA). Collagen-I was extracted from rat-tails (acetic acid extraction)[94] and quantified using the modified Lowry method[95]. Glass coverslips (12 mm) were cleaned with 7X cleaning solution (MP Biomedicals), treated with plasma, silanized with 3-aminopropyltriethoxysilane (APTES), and coated with 0.1 mg/ml extracted collagen. A laser engraver (Epilog) was used to print stencils on 250 µm thick silicone sheets (PDMS), which were then successively cleaned in 70% isopropyl alcohol and Milli-Q water, and air-dried. Cleaned stencils were then aligned on top of collagen-coated coverslips, and this assembly was treated with 0.2% pluronic F-127 (Sigma) for 15 minutes, followed by PBS and DMEM rinses. The stencil-overlaid coverslips were placed in 24-well plates. MCF-7 cells were seeded at a density of 300,000 cells per micropattern in the 24-well plates and allowed to adhere onto the circular islands within the micropatterns for 5 hours. Next, the micropatterns were rinsed in DMEM to remove excessive cancer cells. After overnight incubation, stencils were removed from the coverslips and micropatterns were rinsed thoroughly in DMEM. BMSCs were seeded (at densities ranging from 25,000 to 100,000 cells per micropattern) and rinsed off from the cancer island by thorough DMEM rinsing within 30 minutes of seeding to allow for adhesion in the surrounding areas without contaminating the cancer cell region (day 0). The micropatterned cells were cultured for 4 days before the subsequent analysis.

Imaging of the mitochondrial membrane potential ($\Delta\Psi_m$) in the μTSA. Day 4 micropatterns were stained at 37 °C for 30 minutes with the mitochondrial membrane dye, tetramethylrhodamine methyl ester, (30 nM in complete medium; TMRM, Life Technologies). Following incubation, micropatterns were rinsed and immediately imaged in PBS using a Nikon Eclipse Ti inverted fluorescence microscope.

Immunofluorescence. Day 4 micropatterns were fixed with 4% paraformaldehyde (Electron Microscopy Sciences) at room temperature for 15 minutes, rinsed with PBS, and permeabilized with 0.1% Triton X-100 (Fisher Scientific) for 10 minutes. Micropatterns were then blocked with 4% bovine serum albumin (GE Healthcare), either for one hour at room temperature or overnight at 4 °C, followed by incubation with the primary antibody for 2 hours at room temperature, three PBS rinses and incubation with the respective secondary antibodies at room temperature for 1 hour. Micropatterns were then rinsed three times with PBS and once with milli-Q water, mounted onto glass slides using FluoroGel II (Electron Microscopy Sciences), and imaged with the Nikon Eclipse Ti inverted microscope and/or the Nikon confocal microscope.

Metabolic imaging (NAD(P)H and FAD fluorescence). A Zeiss LSM-780 inverted confocal microscope coupled to a Ti-Sapphire laser system and an A320 FastFLIM FLIMbox[96] was used to determine the fluorescence intensities of NADH and FAD in day 4 MCF-7/BMSC μTSA. Image processing and quantification were performed using a customized code in Python2.7.

Laser capture microdissection (LCM) and RNA sequencing. Day 4 micropatterns were fixed in 100% ethanol, serially rehydrated in 75% ethanol and water, and stained with the Histogene Staining Solution (Applied Biosystems). The samples were then serially rinsed and dehydrated in water, 75%, 95%, and 100% ethanol, submerged in xylene, and air-dried immediately before being mounted onto glass slides with cell side up for LCM. The ArcturusXT Laser Capture Microdissection System was used to extract MCF-7 cells at the centers and edges of the MCF-7-BMSC μTSA. RNA from the micro-dissected cells was extracted using the PicoPure RNA Isolation Kit (Arcturus) following the manufacturer's instructions. RNA concentrations were determined by absorbance on a NanoDrop One spectrophotometer and Qubit (ThermoFisher). RNA integrity was determined using the Agilent 2100 Bioanalyzer and RNA 6000 Nano Chip kit. Only samples with an RNA Integrity Number (RIN) score greater than 7 were used. Following mRNA purification from total RNA using poly-A selection, a cDNA library was prepared using Illumina TruSeq Stranded mRNA Library Prep kit. The cDNA library quality was checked using the Agilent 2100 Bioanalyzer and D1000 DNA Chip kit. Samples were run on the Illumina NextSeq500 platform using the High Output Sequencing Kit v2 (150 cycles, 2 × 75 bp read length, 20 million reads per sample). Library preparation and sequencing were performed by the Single Cell, Sequencing, and CyTOF (SC^2) Core (Children's Hospital of Los Angeles, Los Angeles, CA).

Gene set enrichment analysis (GSEA). Before analysis, raw FASTQ files from RNA-sequencing were checked for read quality using FASTQC. Next, reads were mapped to the most recent *Homo sapiens* reference genome (GRCh38) using the HISAT2 splice aligner[97]. After alignment, mapped reads were counted with R using the Rsubread Bioconductor package[98]. Read counts were arranged into a count matrix and differentially expressed gene (DEG) analysis was performed using DESeq. 2 in R[99]. A pairwise comparison using the Wald Chi-Squared test was employed to contrast gene expression within our two groups (μTSA interface versus center) and genes were subsequently ranked based on comparison significance ($-\log_{10}$(nominal p-value)*LFC direction; where LFC is the log fold change). GSEA was then conducted under default settings to identify the coordinated enrichment of functionally linked genes[100,101]. Briefly, the GSEA algorithm walks through the pre-ranked dataset and calculates a running enrichment score (ES) by increasing the ES when a dataset gene is found to be a member of the gene set of interest and decreasing the ES if it is not. A gene set is identified as enriched when the final ES is high and weighted towards a single phenotype. Statistical significance is determined by comparing the ES to the ES_{null} obtained by permutating the ranked dataset 1000 times and recalculating the ES. Nominal p-values are then adjusted for multiple testing correction through the false discovery rate (FDR) Benjamini-Hochberg method[102]. Gene sets with an $FDR < 0.25$ were considered as significantly enriched. Functionally linked gene sets were obtained from the Hallmark[103], KEGG, and Gene Ontology[104] collections compiled in Molecular Signatures Database (MSigDB)[100].

Mechanical constraints. A microcontact printing approach was used to create a PDMS barrier for the complete mechanical constraint in μTSA. To create a mold for the stamps, circular outlines (2 mm in diameter) were cut on a 140 μm thick protective film tape (Patco) with a desktop craft cutter (Silhouette Cameo). The circular tape cutouts were then transferred onto the bottom of 150 mm diameter petri dishes, and covered with a 1 mm-thick layer of PDMS (curing agent:base = 1:10, Sylgard 184, Dow Corning), degassed, and cured at 65 °C. The cured PDMS layer was then cut with a biopsy punch (10 mm in diameter) to obtain PDMS stamps with the 2 mm concave circular region at their center replica-molded from the tape cutouts. To create a PDMS barrier, a thin layer of freshly mixed and degassed PDMS was spin-coated on a round 18 mm-diameter glass coverslip. A stamp was placed on top of the thin PDMS layer, inked with PDMS, and then transferred onto a collagen-coated coverslip. The stamp was then removed and discarded. The transferred PDMS layer was cured overnight at room temperature. Before use, the coverslips were incubated in 0.2% pluronic F-127 (Sigma) for 15 minutes followed by rinses with PBS and DMEM. MCF-7 cells were then seeded to create completely confined tumor micropattern.

***In vivo* metastasis model.** All animal studies were carried out in accordance with the recommendations in the Guide for the Care and Use of Laboratory Animals of the National Institutes of Health. The protocol was approved by the Institutional Animal Care and Use Committee of the University of Southern California. MCF-7 and MDA-MB-231 breast cancer cells (ATCC), stably transduced with a GFP/luciferase construct[62,63], were stained with TMRM or DiIC1(5) (MitoProbe DiIC1(5) Assay Kit, Invitrogen) as a marker of mitochondrial membrane potential and sorted on the BD FACSAria I cell sorter (Flow Cytometry Core Facility, USC). Sorted cells were inoculated into NSG (NOD.Cg-*Prkdc*^{scid} *Il2rg*^{tm1Wjl}*/SzJ*) mice through tail vein injections (300,000 cells per mouse for MCF-7 and 100,000 cells per mouse for MDA-MB-231). For the MCF-7 study, mice were implanted with 17β-estradiol 90-day release pellets (0.36 mg/pellet), using a sterile trochar 24 hours prior to the injections. After five weeks (for MCF-7 cells) or four weeks (for MDA-MB-231 cells), the animals were euthanized and their lungs were harvested, ground, and assayed for metastatic tumor content using a Luciferase Assay System (Promega)[17].

Statistical analysis. Other than the RNA sequencing data (see above), all data are presented as mean ± standard deviation (SD), as stated in the figure legends. Statistical significance was assessed using the Welch's t-test (parametric) and Mann-Whitney (non-parametric) for pair-wise comparison, and ordinary 1-way ANOVA for comparison between multiple ($\geq$3) conditions; $p < 0.05$ was considered as significant.

Data Availability

The raw RNA sequencing data files generated during the present study have been deposited in the NCBI Sequence Read Archive (SRA Bioproject ID PRJNA523041).

References

1. Siegel, R. L., Miller, K. D. & Jemal, A. Cancer Statistics, 2018. *CA Cancer J Clin.* **67**, 7–30 (2018).
2. Morais, R. *et al*. Tumor-forming Ability in Athymic Nude Mice of Human Cell Lines Devoid of Mitochondrial DNA. *Cancer Res.* **54**, 3889–3896 (1994).
3. Dong, L. *et al*. Horizontal transfer of whole mitochondria restores tumorigenic potential in mitochondrial DNA-deficient cancer cells. *Elife* **6**, 1–22 (2017).
4. Tan, A. S. *et al*. Mitochondrial genome acquisition restores respiratory function and tumorigenic potential of cancer cells without mitochondrial DNA. *Cell Metab.* **21**, 81–94 (2015).
5. Dang, L. *et al*. Cancer-associated IDH1 mutations produce 2-hydroxyglutarate. *Nature* **462**, 739–744 (2009).
6. Sciacovelli, M. *et al*. Fumarate is an epigenetic modifier that elicits epithelial-to-mesenchymal transition. *Nature* **537**, 544–547 (2016).
7. Yang, J. & Weinberg, R. A. Epithelial-Mesenchymal Transition: At the Crossroads of Development and Tumor Metastasis. *Dev. Cell*, 818–829, (2008).
8. Porporato, P. E., Filigheddu, N., Pedro, J. M. B.-S., Kroemer, G. & Galluzzi, L. Mitochondrial metabolism and cancer. *Cell Res.* **28**, 265–280 (2017).
9. Heerdt, B. G., Houston, M. A., Anthony, G. M. & Augenlicht, L. H. Mitochondrial membrane potential in the coordination of p53-independent proliferation and apoptosis pathways in human colonic carcinoma cells. *Cancer Res.* **58**, 2869–2875 (1998).
10. Heerdt, B. G., Houston, M. A. & Augenlicht, L. H. The intrinsic mitochondrial membrane potential of colonic carcinoma cells is linked to the probability of tumor progression. *Cancer Res.* **65**, 9861–9867 (2005).
11. Kuwahara, Y. *et al*. The Involvement of Mitochondrial Membrane Potential in Cross-Resistance Between Radiation and Docetaxel. *Int. J. Radiat. Oncol. Biol. Phys.* **96**, 556–565 (2016).
12. Schieke, S. M. *et al*. Mitochondrial metabolism modulates differentiation and teratoma formation capacity in mouse embryonic stem cells. *J. Biol. Chem.* **283**, 28506–28512 (2008).
13. Lebleu, V. S. *et al*. PGC-1α mediates mitochondrial biogenesis and oxidative phosphorylation in cancer cells to promote metastasis. *Nat. Cell Biol.* **16**, 992–1003 (2014).
14. Quail, D. F. & Joyce, J. A. Microenvironmental regulation of tumor progression and metastasis. *Nat. Med.* **19**, 1423–1437 (2013).
15. Cunha, G. R. Role of mesenchymal-epithelial interactions in normal and abnormal development of the mammary gland and prostate. *Cancer* **74**, 1030–1044 (1994).
16. Ronnov-Jessen, L., Petersen, O. W. & Bissell, M. J. Cellular changes involved in conversion of normal to malignant breast: importance of the stromal reaction. *Physiol. Rev.* **76**, 69–125 (1996).
17. Shen, K. *et al*. Resolving cancer-stroma interfacial signalling and interventions with micropatterned tumour-stromal assays. *Nat. Commun.* **5**, 1–11 (2014).
18. Sgroi, D. C. Preinvasive Breast Cancer. *Annu. Rev. Pathol. Mech. Dis.* **5**, 193–221 (2010).
19. Jain, R. K., Martin, J. D. & Stylianopoulos, T. The Role of Mechanical Forces in Tumor Growth and Therapy. *Annu. Rev. Biomed. Eng.* **16**, 321–346 (2014).
20. Tajan, M. & Vousden, K. H. The Quid Pro Quo of the Tumor/Stromal Interaction. *Cell Metab.* **24**, 645–646 (2016).
21. Lyssiotis, C. A. & Kimmelman, A. C. Metabolic Interactions in the Tumor Microenvironment. *Trends in Cell Biology* **27**, 863–875 (2017).
22. Spill, F., Reynolds, D. S., Kamm, R. D. & Zaman, M. H. Impact of the physical microenvironment on tumor progression and metastasis. *Curr. Opin. Biotechnol.* **40**, 41–48 (2016).
23. Stylianopoulos, T. *et al*. Causes, consequences, and remedies for growth-induced solid stress in murine and human tumors. *Proc. Natl. Acad. Sci.* **109**, 15101–15108 (2012).
24. Chaudhuri, P. K., Low, B. C. & Lim, C. T. Mechanobiology of Tumor Growth. *Chem. Rev.* **118**, 6499–6515 (2018).
25. Carey, S. P., D'Alfonso, T. M., Shin, S. J. & Reinhart-King, C. A. Mechanobiology of tumor invasion: Engineering meets oncology. *Crit. Rev. Oncol. Hematol.* **83**, 170–183 (2012).
26. Tse, J. M. *et al*. Mechanical compression drives cancer cells toward invasive phenotype. *Proc. Natl. Acad. Sci.* **109**, 911–916 (2012).
27. Tomasek, J. J., Gabbiani, G., Hinz, B., Chaponnier, C. & Brown, R. A. Myofibroblasts and mechano-regulation of connective tissue remodelling. *Nat. Rev. Mol. Cell Biol.* **3**, 349–363 (2002).
28. Bartolák-Suki, E., Imsirovic, J., Nishibori, Y., Krishnan, R. & Suki, B. Regulation of mitochondrial structure and dynamics by the cytoskeleton and mechanical factors. *Int. J. Mol. Sci.* **18**, 7–11 (2017).
29. Moore, A. S., Wong, Y. C., Simpson, C. L. & Holzbaur, E. L. F. Dynamic actin cycling through mitochondrial subpopulations locally regulates the fission-fusion balance within mitochondrial networks. *Nat. Commun.* **7**, 1–13 (2016).

30. Karnoub, A. E. *et al*. Mesenchymal stem cells within tumour stroma promote breast cancer metastasis. *Nature* **449**, 557–563 (2007).
31. Consortium, T. G. O. Expansion of the Gene Ontology knowledgebase and resources. *Nucleic Acids Res.* **45**, 331–338 (2017).
32. Ashburner, M. *et al*. Gene Ontology: tool for the unification of biology. *Nat. Genet.* **25**, 25–29 (2000).
33. Kanehisa, M. & Goto, S. KEGG: Kyoto Encyclopedia of Genes and Genomes. *Nucleic Acids Res.* **28**, 27–30 (2000).
34. Kanehisa, M., Furumichi, M., Tanabe, M., Sato, Y. & Morishima, K. KEGG: new perspectives on genomes, pathways, diseases and drugs. *Nucleic Acids Res.* **45**, 353–361 (2017).
35. Kanehisa, M., Sato, Y., Kawashima, M., Furumichi, M. & Tanabe, M. KEGG as a reference resource for gene and protein annotation. *Nucleic Acids Res.* **44**, 457–462 (2016).
36. Wei, T. W. *et al*. Protein arginine methyltransferase 5 is a potential oncoprotein that upregulates G1 cyclins/cyclin-dependent kinases and the phosphoinositide 3-kinase/AKT signaling cascade. *Cancer Sci.* **103**, 1640–1650 (2012).
37. Wang, Y. *et al*. Gene-expression profiles to predict distant metastasis of lymph-node-negative primary breast cancer. *Lancet* **365**, 671–679 (2005).
38. Anastassiou, D. *et al*. Human cancer cells express Slug-based epithelial-mesenchymal transition gene expression signature obtained *in vivo*. *BMC Cancer* **11**(529), 1–9 (2011).
39. Cunningham, J. T. *et al*. mTOR controls mitochondrial oxidative function through a YY1-PGC-1α transcriptional complex. *Nature* **450**, 736–740 (2007).
40. Scaduto, R. C. & Grotyohann, L. W. Measurement of mitochondrial membrane potential using fluorescent rhodamine derivatives. *Biophys. J.* **76**, 469–477 (1999).
41. Perry, S. W., Norman, J. P., Barbieri, J., Brown, E. B. & Gelbard, H. A. Mitochondrial membrane potential probes and the proton gradient: A practical usage guide. *Biotechniques* **50**, 98–115 (2011).
42. Burbulla, L. F. *et al*. Mitochondrial proteolytic stress induced by loss of mortalin function is rescued by Parkin and PINK1. *Cell Death Dis.* **5**, 1–19 (2014).
43. De Ruyck, J. *et al*. Towards the understanding of the absorption spectra of NAD(P)H/NAD(P)+ as a common indicator of dehydrogenase enzymatic activity. *Chem. Phys. Lett.* **450**, 119–122 (2007).
44. Blacker, T. S. & Duchen, M. R. Investigating mitochondrial redox state using NADH and NADPH autofluorescence. *Free Radic. Biol. Med.* **100**, 53–65 (2016).
45. Alhallak, K. *et al*. Optical redox ratio identifies metastatic potential-dependent changes in breast cancer cell metabolism. *Clin. Oncol* **34**, 2303–2311 (2016).
46. Dumollard, R., Ward, Z., Carroll, J. & Duchen, M. R. Regulation of redox metabolism in the mouse oocyte and embryo. *Development* **134**, 455–465 (2007).
47. Huang, J., Wu, S., Barrera, J., Matthews, K. & Pan, D. The Hippo Signaling Pathway Coordinately Regulates Cell Proliferation and Apoptosis by Inactivating Yorkie, the Drosophila Homolog of YAP. *Cell* **122**, 421–434 (2005).
48. Pan, D. The hippo signaling pathway in development and cancer. *Dev. Cell* **19**, 491–505 (2010).
49. Dupont, S. *et al*. Role of YAP/TAZ in mechanotransduction. *Nature* **474**, 179–184 (2011).
50. Das, A., Fischer, R. S., Pan, D. & Waterman, C. M. YAP nuclear localization in the absence of cell-cell contact is mediated by a filamentous actin-dependent, Myosin IIand Phospho-YAP-independent pathway during extracellular matrix mechanosensing. *J. Biol. Chem.* **291**, 6096–6110 (2016).
51. Hanahan, D. & Weinberg, R. A. Hallmarks of cancer: The next generation. *Cell* **144**, 646–674 (2011).
52. Monod, J. The growth of bacterial cultures. *Annu. Rev. Microbiol.* **3**, 371–394 (1949).
53. Zhao, B. *et al*. Inactivation of YAP oncoprotein by the Hippo pathway is involved in cell contact inhibition and tissue growth control. *Genes Dev.* **21**, 2747–2761 (2007).
54. Svoboda, K. K. H., Moessner, P., Field, T. & Acevedo, J. ROCK Inhibitor (Y27632) Increases Apoptosis and Disrupts the Actin Cortical Mat in Embryonic Avian Corneal Epithelium. *Dev. Dyn.* **229**, 579–590 (2009).
55. Coue, M., Brenner, S. L., Spector, I. & Korn, E. D. Inhibition of actin polymerization by latrunculin A. *FEBS Lett.* **213**, 316–318 (1987).
56. Furukawa, K. T., Yamashita, K., Sakurai, N. & Ohno, S. The Epithelial Circumferential Actin Belt Regulates YAP/TAZ through Nucleocytoplasmic Shuttling of Merlin. *Cell Rep.* **20**, 1435–1447 (2017).
57. Omelchenko, T., Vasiliev, J. M., Gelfand, I. M., Feder, H. H. & Bonder, E. M. Mechanisms of polarization of the shape of fibroblasts and epitheliocytes: Separation of the roles of microtubules and Rho-dependent actin-myosin contractility. *Proc. Natl. Acad. Sci.* **99**, 10452–10457 (2002).
58. Harris, A. R., Jreij, P. & Fletcher, D. A. Mechanotransduction by the Actin Cytoskeleton: Converting Mechanical Stimuli into Biochemical Signals. *Annu. Rev. Biophys.* **47**, 617–631 (2018).
59. Ohashi, K., Fujiwara, S. & Mizuno, K. Roles of the cytoskeleton, cell adhesion and rho signalling in mechanosensing and mechanotransduction. *J. Biochem.* **161**, 245–254 (2017).
60. Karmali, P. P. *et al*. Metastasis of tumor cells is enhanced by downregulation of Bit1. *PLoS One* **6** (2011).
61. Barkan, D. *et al*. Inhibition of metastatic outgrowth from single dormant tumor cells by targeting the cytoskeleton. *Cancer Res.* **68**, 6241–6250 (2008).
62. Lee, J., Wang, J. B., Bersani, F. & Parekkadan, B. Capture and printing of fixed stromal cell membranes for bioactive display on PDMS surfaces. *Langmuir* **29**, 10611–10616 (2013).
63. Iriondo, O. *et al*. TAK1 mediates microenvironment-triggered autocrine signals and promotes triple-negative breast cancer lung metastasis. *Nat. Commun.* **9**, 1–10 (2018).
64. Xu, H. N., Tchou, J. & Li, L. Z. Redox Imaging of Human Breast Cancer Core Biopsies. A Preliminary Investigation. *Acad. Radiol.* **20**, 764–768 (2013).
65. Xu, H. N., Tchou, J., Feng, M., Zhao, H. & Li, L. Z. Optical redox imaging indices discriminate human breast cancer from normal tissues. *J. Biomed. Opt.* **21**, 1–8 (2016).
66. Li, L. Z. *et al*. Quantitative magnetic resonance and optical imaging biomarkers of melanoma metastatic potential. *Proc. Natl. Acad. Sci.* **106**, 6608–6613 (2009).
67. Ralph, S. J., Rodríguez-Enríquez, S., Neuzil, J., Saavedra, E. & Moreno-Sánchez, R. The causes of cancer revisited: 'Mitochondrial malignancy' and ROS-induced oncogenic transformation - Why mitochondria are targets for cancer therapy. *Mol. Aspects Med.* **31**, 145–170 (2010).
68. Martinez-Outschoorn, U. E. *et al*. Stromal-epithelial metabolic coupling in cancer: Integrating autophagy and metabolism in the tumor microenvironment. *Int. J. Biochem. Cell Biol.* **43**, 1045–1051 (2011).
69. Morris, B. A. *et al*. Collagen Matrix Density Drives the Metabolic Shift in Breast Cancer Cells. *EBioMedicine* **13**, 146–156 (2016).
70. Scharping, N. E. *et al*. The Tumor Microenvironment Represses T Cell Mitochondrial Biogenesis to Drive Intratumoral T Cell Metabolic Insufficiency and Dysfunction. *Immunity* **45**, 374–388 (2016).
71. van Brussel, A. S. A. *et al*. Hypoxia-Targeting Fluorescent Nanobodies for Optical Molecular Imaging of Pre-Invasive Breast Cancer. *Mol. Imaging Biol.* **18**, 535–544 (2016).
72. Malandrino, A., Mak, M., Kamm, R. D. & Moeendarbary, E. Complex mechanics of the heterogeneous extracellular matrix in cancer. *Extrem. Mech. Lett.* **21**, 25–34 (2018).
73. Pickup, M. W., Mouw, J. K. & Weaver, V. M. The extracellular matrix modulates the hallmarks of cancer. *EMBO Rep.* **15**, 1243–1253 (2014).

74. DelNero, P., Hopkins, B. D., Cantley, L. C. & Fischbach, C. Cancer metabolism gets physical. *Sci Transl Med* **10**, 1–7 (2018).
75. Hu, H. *et al*. Phosphoinositide 3-Kinase Regulates Glycolysis through Mobilization of Aldolase from the Actin Cytoskeleton. *Cell* **164**, 433–446 (2016).
76. Chan, Y. H. M. & Marshall, W. F. Scaling properties of cell and organelle size. *Organogenesis* **6**, 88–96 (2010).
77. Miettinen, T. P. & Björklund, M. Cellular Allometry of Mitochondrial Functionality Establishes the Optimal Cell Size. *Dev. Cell* **39**, 370–382 (2016).
78. Susanne, M. R. *et al*. Mitochondrial Network Size Scaling in Budding Yeast. *Science (80-.)*. **338**, 822–824 (2012).
79. Nagaraj, R. *et al*. Control of mitochondrial structure and function by the Yorkie / YAP oncogenic pathway. *Genes Dev.* **26**, 2027–2037 (2012).
80. von Eyss, B. *et al*. A MYC-Driven Change in Mitochondrial Dynamics Limits YAP/TAZ Function in Mammary Epithelial Cells and Breast Cancer. *Cancer Cell* **28**, 743–757 (2015).
81. Xie, X., Venit, T., Drou, N. & Percipalle, P. In Mitochondria β-Actin Regulates mtDNA Transcription and Is Required for Mitochondrial Quality Control. *iScience* **3**, 226–237 (2018).
82. Porazinski, S. *et al*. YAP is essential for tissue tension to ensure vertebrate 3D body shape. *Nature* **521**, 217–221 (2015).
83. Qiao, Y. *et al*. YAP Regulates Actin Dynamics through ARHGAP29 and Promotes Metastasis. *CellReports* **19**, 1495–1502 (2017).
84. Amano, M., Nakayama, M. & Kaibuchi, K. Rho-Kinase/ROCK: A Key Regulator of the Cytoskeleton and Cell Polarity. *Cytoskeleton* **67**, 545–554 (2010).
85. Fiaschi, T. *et al*. Reciprocal metabolic reprogramming through lactate shuttle coordinately influences tumor-stroma interplay. *Cancer Res.* **72**, 5130–40 (2012).
86. Sonveaux, P. *et al*. Targeting lactate-fueled respiration selectively kills hypoxic tumor cells in mice. *J. Clin. Invest.* **118**, 3930–3942 (2008).
87. Gao, D., Rahbar, R. & Fish, E. N. CCL5 activation of CCR5 regulates cell metabolism to enhance proliferation of breast cancer cells. *Open Biol.* **6**(160122), 1–13 (2016).
88. Bronzert, D. A. *et al*. Synthesis and secretion of platelet-derived growth factor by human breast cancer cell lines. *Proc Natl Acad Sci USA* **84**, 5763–7 (1987).
89. Tobar, N. *et al*. Soluble MMP-14 produced by bone marrow-derived stromal cells sheds epithelial endoglin modulating the migratory properties of human breast cancer cells. *Carcinogenesis* **35**, 1770–1779 (2014).
90. Haslam, S. Z., Counterman, L. J. & Nummy, K. A. Epithelial-Stromal Cell Interactions and Breast Cancer. *Adv. Mol. Cell Biol.* **7**, 115–130 (1993).
91. Kalluri, R. The biology and function of fibroblasts in cancer. *Nature Reviews Cancer* **16**, 582–598 (2016).
92. Welsh, J. E. *Animal Models for Studying Prevention and Treatment of Breast Cancer. Animal Models for the Study of Human Disease*, https://doi.org/10.1016/B978-0-12-415894-8.00040-3 (Elsevier, 2013).
93. Parekkadan, B. *et al*. Mesenchymal stem cell-derived molecules reverse fulminant hepatic failure. *PLoS One* **2**, 1–6 (2007).
94. Rajan, N., Habermehl, J., Coté, M. F., Doillon, C. J. & Mantovani, D. Preparation of ready-to-use, storable and reconstituted type I collagen from rat tail tendon for tissue engineering applications. *Nat. Protoc.* **1**, 2753–2758 (2007).
95. Komsa-Penkova, R., Spirova, R. & Bechev, B. Modification of Lowry's method for collagen concentration measurement. *Biochem. Biophys. methods* **32**, 33–43 (1996).
96. Browne, A. W. *et al*. Structural and functional characterization of human stem-cell-derived retinal organoids by live imaging. *Investig. Ophthalmol. Vis. Sci.* **58**, 3311–3318 (2017).
97. Pertea, M., Kim, D., Pertea, G. M., Leek, J. T. & Salzberg, S. L. Transcript-level expression analysis of RNA-seq experiments with HISAT, StringTie and Ballgown. *Nat. Protoc.* **11**, 1650–1667 (2016).
98. Liao, Y., Smyth, G. K. & Shi, W. The Subread aligner: Fast, accurate and scalable read mapping by seed-and-vote. *Nucleic Acids Res.* **41** (2013).
99. Love, M. I., Huber, W. & Anders, S. Moderated estimation of fold change and dispersion for RNA-seq data with DESeq. 2. *Genome Biol.* **15**, 1–21 (2014).
100. Subramanian, A. *et al*. Gene set enrichment analysis: A knowledge-based approach for interpreting genome-wide expression profiles. *Proc. Natl. Acad. Sci.* **102**, 15545–15550 (2005).
101. Mootha, V. K. *et al*. PGC-1 alpha-responsive genes involved in oxidative phosphorylation are coordinately downregulated in human diabetes. *Nat. Genet.* **34**, 267–273 (2003).
102. Benjamini, Y. & Hochberg, Y. Controlling the False Discovery Rate: A Practical and Powerful Approach to Multiple. *Testing. J. R. Stat. Soc.* **57**, 289–300 (1995).
103. Liberzon, A. *et al*. The Molecular Signatures Database Hallmark Gene Set Collection. *Cell Syst.* **1**, 417–425 (2015).
104. Liberzon, A. *et al*. Molecular signatures database (MSigDB) 3.0. *Bioinformatics* **27**, 1739–1740 (2011).

Acknowledgements

We thank Dr. Scott Fraser for providing Zeiss LSM-780 two-photon confocal microscope for redox imaging; Dr. Megan McCain for providing Nikon C2 confocal microscope for the non-redox confocal imaging. We also thank Drs. Long Hung and Fan Li for their RNA-seq services at the Single Cell, Sequencing, and CyTOF (SC^2) Core at Children's Hospital of Los Angeles, Los Angeles, CA; Dr. Yong-Hwee Eddie Loh at USC Libraries Bioinformatics Service for assisting with RNA-seq data analysis. We thank Dr. Martine Torres for her critical reading of the manuscript and editorial assistance. This work was supported by NIH NIBIB Trailblazer Award R21EB024748, USC Viterbi School of Engineering, STOP CANCER Marni Levine Memorial Research Career Development Award, Phi Beta Psi Charity Trust, Rose Hills Fellowship, USC Provost's PhD Fellowship, USC Diversity, Inclusion and Access (DIA) Fellowship, USC Women in Science and Engineering (WiSE) Fellowship, and USC Undergraduate Research Associates Program. It is also in part supported through shared resources by award number P30CA014089 from the National Cancer Institute at the NIH.

Author Contributions

H.M.B. contributed to the design of the study, performed experiments, analyzed data, and wrote the manuscript. H.P.T. prepared samples for RNA-seq and analyzed the RNA-seq data. H.Z. performed quantification of Optical Redox Ratio (ORR) images. Y.A. acquired ORR images. D.K. performed the *in vivo* study. K.N. and C.F.M. assisted with cell culture and micropatterning. J.H. assisted with organ harvest for the *in vivo* study. M.Y. performed the *in vivo* studies and interpreted the data. K.S. conceived and designed the study, provided funding, analyzed and interpreted data, and wrote the manuscript.

Additional Information

Supplementary information accompanies this paper at https://doi.org/10.1038/s41598-019-47593-8.

Competing Interests: The authors declare no competing interests.